

Capture and re-entrainment of microdroplets on fibers

S. Abishek,^{1,2} R. Mead-Hunter,^{1,2} A. J. C. King,^{2,3} and B. J. Mullins^{1,2}

¹*Occupation, Environment and Safety, School of Public Health, Curtin University, Perth, Western Australia 6102, Australia*

²*Fluid Dynamics Research Group and The Curtin Institute for Computation, Curtin University, Perth, Western Australia 6102, Australia*

³*School of Civil and Mechanical Engineering, Curtin University, Perth, Western Australia 6102, Australia*



(Received 10 August 2018; revised manuscript received 30 August 2019; published 21 October 2019)

The capture of liquid microdroplets on fibers, webs, and surfaces is important in a range of natural and industrial processes. One such application is the fibrous filtration of aerosols. Contact angle and wetting dynamics have a significant influence on capture and re-entrainment, yet there is no comprehensive model that accounts for these properties and their influence on capture efficiency. In this study, a series of computational simulations using liquid droplets and air are carried out to investigate the influence of equilibrium and dynamic contact angles on the capture and re-entrainment of mist droplets. A range of operating conditions for droplet-fiber diameter ratios, flow velocities, and contact angles, encapsulating both super-oleophilic and super-oleophobic media, are considered. All simulations are carried out using the volume of fluid (VOF) interface capturing approach in the finite volume solver *interFoam* within *OpenFOAM*. The physics of microdroplet impacting on a fiber is discussed and three distinct regimes for the spreading of the droplet around the fiber—inertia, capillary, and stagnation pressure controlled—are identified. It was found that the classification of filtration media for any fluid system, rather broadly as philic or phobic, based on the equilibrium contact angle alone may be insufficient for two reasons: (i) the characteristics of droplet-fiber interaction, including capture or re-entrainment, differs significantly over the range of contact angles for both philic and phobic media; and more importantly (ii) equilibrium contact angle plays little role in the initial stages of the droplet-fiber interaction that predominantly dictates the fate of the droplet. On the contrary, it is the contact angle dynamics that influences the initial stages of droplet impact on fibers, while commercial filters are seldom characterized based on this property. The isolated influence of equilibrium, advancing and receding contact angles on the potential mechanisms that can result in full or partial capture or re-entrainment are highlighted. The influence of equilibrium and advancing and receding hystereses are summarized in the form of a capture-regime map that shows four distinct regimes: (i) likely capture, (ii) likely re-entrainment with minimal or no capture, (iii) receding contact angle assisted partial or full capture, and (iv) advancing contact angle inhibited partial or full re-entrainment.

DOI: [10.1103/PhysRevE.100.042803](https://doi.org/10.1103/PhysRevE.100.042803)

I. INTRODUCTION

Recovery of liquid aerosols is of significant importance in a variety of industrial and automotive applications for economic and toxicological reasons. The underlying processes are also relevant to fuel cells, tissue culture scaffolds, and natural processes such as coalescence of dew and sea mist on surfaces such as spider webs. Removal of such mist is typically accomplished by using highly porous fibrous, knitted, or foam filters [1,2]. The process of mist filtration is characterized by initial capture of aerosols in a dry filter, coalescence and redistribution of the collected fluid into larger structures, and finally, an equilibrium state of fluid saturation with continuous balanced collection and drainage or re-entrainment. Some filters such as respirators operate predominantly in the initial capture state with low levels of fluid saturation. Most industrial oil-mist filters are oleophilic in nature, while carefully engineered oleophobic media are gaining increasing interest due to the advantages in reduced pressure-drops [3] resulting from enhanced drainage of the captured oil, and potentially greater capture efficiencies [4,5]. The effect of oleophobicity or -philicity of the filter media on the overall filtration efficiency has received some attention [3,6] for conditions of high fluid saturation. However, the capture efficiency in the initial dry

filtration stage is estimated predominantly by the single-fiber efficiency theory (SFE) [7] that was originally developed for dust filtration—with the assumption that a particle sticks to the surface of the filter after contact.

The SFE theory presents a series of equations for each possible mechanism for particle (or droplet) capture. In most liquid aerosol applications the main capture mechanisms are impaction, interception and diffusion, and authors have used a combination of these equations summatively to predict the overall collection efficiency [7]. There have, however, been a number of discrepancies noted between theory and experiment [2,4,8,9] which are usually explained by the differences between “real” filters used in experiments (and applications) and the “idealized” geometries, operating conditions and physical processes considered to develop the SFE models. There are also several expressions available for each capture mechanism, the choice of which will ultimately influence the calculated efficiency [2,10]. These models often include empirically derived terms, which may give excellent agreement for the specific filters used to develop them, however, are less applicable, when the filter properties differ significantly. This was illustrated conclusively in Mead-Hunter *et al.* [2]. There is also the added influence of liquid coalescence and

redistribution within the filter [2] during mist filtration, as opposed to solid particles. This is, however, less significant during the initial capture stage.

For purely initial capture, the equations in SFE theory encapsulates the major capture mechanisms in play (impaction, interception and diffusion), but fails to account for processes that can lead to the re-entrainment of a particle or droplet that has formerly come in contact with a fiber. This can lead to overestimation of the capture efficiencies. For solid and dust particle filtration, some of the physical processes that result in deviations from SFE theory have been identified and corrections have been proposed for improving the efficacy of predictions. Rebound of solid microparticles on fiber surface is one such process that has received considerable study [11–18], leading to the development of a semiempirical plastic and elastic collision model [15,18] for particle-fiber interactions, accounting for the physical properties of the particle (and substrate). These models have also been implemented in computational frameworks for filtration simulations [19,20]. It would be possible to use these methods to simulate collection of liquid microparticles on fibers, if we could treat the liquid droplet as highly plastic and elastic solids. However, such a treatment would be non-physical and it would be more useful to explicitly resolve the impact forces and deformation in the droplets.

Besides elastic deformation, liquid particles are also subjected to spreading and sliding and rolling around the fiber, based on the wetting (or nonwetting) properties of the liquid-fiber combination, as governed by interfacial tension, equilibrium contact angle and wetting hysteresis [21–26]. These parameters can ultimately play a role in the retention of a captured droplet. In a recent study, Wei *et al.* [4] showed from measurements, using microfiber glass filter coated with perfluoroalkyl acrylic copolymer, that super-oleophobicity can also augment the filtration efficiency. A dynamic “bounce-collide-drain” mechanism was proposed [4] to explain this counterintuitive enhancement in the efficiency resulting from the superoleophobicity. However, there is yet no comprehensive model characterizing the mist-fiber interactions accounting for the wide possibilities in contact angles and associated hysteresis [27,28] that can arise from the gamut of materials (and coatings)—including metal, polymer, cellulose, or glass—used to make filtration media. These terms therefore offer additional explanation as to why there is deviation between SFE predicted and experimentally measured efficiencies for the filtration of liquid aerosols in the initial stages of filtration. The detailed understanding of the role of the contact angle on droplet capture (and retention) will therefore help to improve efficiency prediction, through the incorporation of new physical terms, rather than additional (nonphysical) semi-empirical correction factors.

While the influence of contact angle dynamics on the droplet-surface interactions has been widely investigated for flat surfaces [29–34], there is little information in the context of microdroplets on filters. McHale *et al.* [35] also showed that the nature of wetting and equilibrium shapes of sessile droplets on cylindrical surfaces can be quite different from that on flat surfaces, even when the surfaces have identical chemistry. Further, most of the literature on the impact dynamics of droplets on cylinders or wires [36–40]

is restricted to droplets or fiber sizes that are several orders magnitude larger than those relevant to mist filtration applications. The dynamics of interactions at larger scales (or Weber numbers) can predominantly be characterized as inertial interactions, and are significantly different from those at microscales ($We \ll 1$). The low Weber number effects (or capillary dominated modes) such as droplet-sliding and rolling around the fiber, as mentioned earlier, may not occur for larger droplet sizes, and any theory based on the former scales alone may be insufficient in characterizing the droplet-fiber dynamics prevalent in mist filtration processes. One of the motivations for this work is to extend the understanding of the fundamental interactions between droplets and fibers to lower Weber numbers, and conditions involving surface curvature.

Computational fluid dynamics (CFD) is increasingly becoming an integral part of the filter design process [1,41–43] employed in a spectrum of applications spanning from automobile to health care. The efficacy of such CFD is greatly dependent on the accuracy of material properties, such as wettability, used in the simulations. Yet, commercial filters are classified only as philic or phobic, with little or no information on contact angle hysteresis, despite that different combinations of gas and mist and filter media exhibit a spectrum of static and dynamic contact angles. This is because the measurement and characterization of the wetting behavior on micro- or nanofilters is still a significant challenge [44–47], which further limits any visualization of the dynamics of wetting mist droplets on fibers at the micro- or nanoscales. Pore-scale CFD [41–43] using advanced droplet- and interface-tracking techniques provide unique advantages in allowing precise definition of contact angles, and other interfacial properties [48,49], for the characterization of filtration media.

In this study, a series of CFD simulations are carried out using OpenFOAM, to investigate the influence of equilibrium contact angle and wetting dynamics on impaction and interceptional capture, and re-entrainment of a microdroplet on an isolated fiber, under a range of operating conditions for droplet-fiber diameter ratios and flow velocities. Diethylhexyl Sebacate (DEHS) and air are used as the working fluids. The physics of microdroplet impact on a fiber (in a surrounding viscous flow) is discussed, and some of the potential mechanisms that can result in a deviation from single fiber efficiency theory are identified and highlighted through this work.

II. GEOMETRY AND COMPUTATIONAL DOMAIN

A microdroplet of Diethylhexyl Sebacate (DEHS) oil mist of diameter d is carried by a steady stream of air at u_o such that it impacts or intercepts a cylindrical fiber of diameter d_f from an initial location represented by an offset w or apparent overlap s (nondimensionalized as $W = w/d_f$ and $S = s/d_f$), as shown in Fig. 1. The droplet diameter is kept constant in the present study at $d = 2 \mu\text{m}$ which is typical of oil mist generated in many applications, including lubricated machining [52], compressors, or engine crankcase ventilation [53]. The range of other parameters are: $0.25 \leq S (=s/d) \leq 1$, $1 \leq R (=d/d_f) \leq 4$, and $u_o = 0.5 \text{ m/s}$ or 1 m/s resulting in droplet Weber numbers $We = \rho_i u_o^2 d / \sigma = 0.01425$ or 0.057 and fiber Reynolds numbers in the range 0.01667

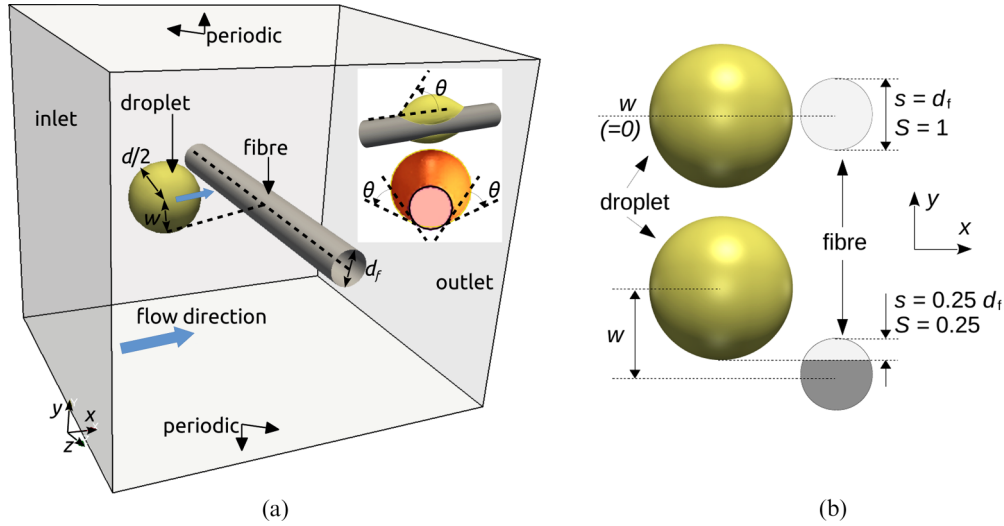


FIG. 1. Schematic of the (a) geometry and computational domain showing fiber orientation, direction of flow and droplet motion, contact angle definitions, and boundary conditions, and (b) representative droplet-fiber impact configurations indicating drop-fiber offsets (w , W) and overlaps (s , S).

$\leq \text{Re} (= \rho_g u_o d_f / \mu_g) \leq 0.133$, where the density (ρ) and dynamic viscosity (μ) of the gas or liquid are designated with subscripts “g” or “l,” respectively, and σ is the surface tension. The wetting characteristics of the droplet on the fiber surface are specified using equilibrium (θ_e), maximum advancing (θ_a), and maximum receding (θ_r) contact angles based on the local velocity (u_s) of the oil-air interface tangential to the filter surface, according to the empirical model from Yokoi *et al.* [29,30]. The properties of DEHS and air used in the simulations are: $\rho_l = 912 \text{ kg/m}^3$, $\mu_l = 0.0228 \text{ Pa s}$, $\rho_g = 1.2 \text{ kg/m}^3$, $\mu_g = 1.8 \times 10^{-5} \text{ Pa s}$, and $\sigma = 0.032 \text{ N/m}$.

The computational simulations are carried out in a domain of size $m \times m \times m$ with the cylindrical fiber placed at the center, and its axis aligned with the z axis. The low Re (based on cylinder or droplet diameter) considered in this study typically correspond to the Stokes flow regime, wherein viscous effects extend to relatively greater lengths from the droplet or cylinder surface; i.e., for $\text{Re} \rightarrow 0$, the relative boundary layer thickness δ/d or $\delta/d_f \rightarrow \infty$. As the controlling length scales for the simulations are d_f or d (for a captured droplet), separate simulations for Stokes flow around a sphere and cylinder were carried out using successively larger domains to identify an adequately large domain size for CFD.

Figure 2 illustrates the variation in the dimensionless pressure coefficient with domain size. The theoretical pressure coefficients during Stokes flows around a cylinder and sphere from Stokes [50] and Kawaguti [51] (given below) are also included in the figure for comparison:

$$c_p = \frac{p - p_\infty}{1/2 \rho u_o^2} = \begin{cases} 6 \cos \varphi / \text{Re} \Rightarrow \text{sphere [50]} \\ \frac{2 \cos \varphi}{\kappa(2\psi-1)} + \frac{(4\psi+1) \cos 2\varphi}{2(2\psi-1)} + O(\kappa) \\ \Rightarrow \text{cylinder [51]} \end{cases} \quad (1)$$

Here, $\kappa = \text{Re}/4$, $\psi = \log(\kappa/2) + \gamma$, $\gamma = 0.57721\dots$ is Euler-Mascheroni constant and φ is the angular position from the upstream stagnation point. The simulations for Figs. 2(a) and 2(b) were carried out using $d = 1 \mu\text{m}$, $d_f = 2 \mu\text{m}$, and $u_o = 1 \text{ m/s}$. It can be seen from the figures that the distribution

of the coefficient of pressure around the cylinder or sphere becomes sufficiently independent of domain size at $m \approx 20 d$ or $m \approx 40 d_f$; the larger of the two values were used for all further simulations reported in this paper.

III. COMPUTATIONAL METHODOLOGY

The governing equations for the conservation of mass and momentum are solved iteratively using the transient, finite-volume solver interFoam in OpenFOAM. The interface between the two fluids (oil and air) is determined by solving for the transport of volume fraction α , where $\alpha = 0$ or 1 represents the computational cell occupied by air or oil, respectively. The solver uses an algebraic volume-of-fluid (VOF) method which is well established for multiphase flow problems of the type considered in this study [42,54–56]. In the VOF technique, a single set of mass and momentum conservation equations (given below) describe the system where the local fluid properties are determined based on the volume fraction:

$$\nabla \cdot \bar{u} = 0, \quad (2)$$

$$\partial(\rho \bar{u})/\partial t + \nabla \cdot (\rho \bar{u} \bar{u}) = -\nabla p + \nabla(\mu \nabla \bar{u}) + \rho \bar{g} + f_\sigma, \quad (3)$$

$$\partial \alpha / \partial t + \nabla \cdot (\alpha \bar{u}) + \nabla[\bar{u}_c \alpha(1 - \alpha)] = 0, \quad (4)$$

where p , g , and t represent pressure, acceleration due to gravity, and time, respectively. In Eq. (4), the compression velocity \bar{u}_c is used to ensure a sharp oil-air interface and reduce numerical smearing. The interfacial surface tension force density (f_σ) is based on the continuum-surface-force model given by Brackbill *et al.* [57] to avoid any numerical issues arising from the discontinuous pressure-jump across the interface [54,58]:

$$f_\sigma = -\sigma[\nabla \cdot (\nabla \alpha_1 / |\nabla \alpha_1|)](\nabla \alpha_1). \quad (5)$$

The conservation equations are solved using the combined iterative PISO-SIMPLE algorithm, and the multidimensional

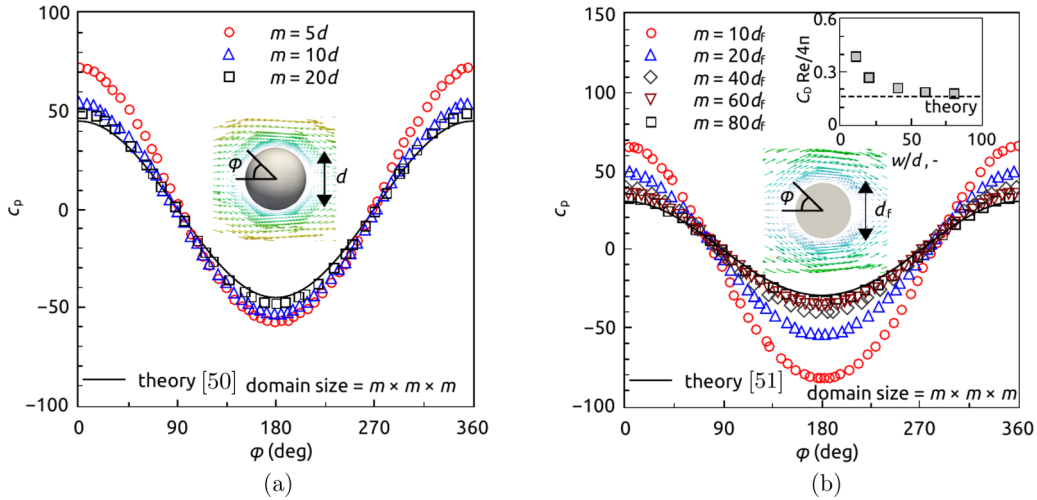


FIG. 2. Influence of domain size on the predicted distribution of pressure coefficient around (a) sphere and (b) cylinder, during Stokes flow ($Re = 0.0667$) and comparison against theory [50,51].

universal limiter with explicit solution (MULES) algorithm for the volume-fraction transport equation [54]. Multiphase flow simulations in the surface tension dominant regimes, which is encompassed in this work, require careful choice of the computational time-step to avoid the notorious issue of parasitic velocities on the oil-air interface [54,59–61]. Hence, an adjustable time-step scheme, which is limited by the flow and interface Courant numbers (<0.2) and additionally by the recommendations of Deshpande *et al.* [54], is employed.

The local contact angle on the fiber surface is modeled based on the interface capillary number ($Ca = \mu u_s / \sigma$) and the limiting advancing (θ_a) or receding (θ_r) contact angles, following Yokoi *et al.* [29,30] as

$$\theta = \begin{cases} \min[\theta_e + (Ca/k_a)^{1/3}, \theta_a] & \text{if } u_s \geq 0 \\ \max[\theta_e + (Ca/k_r)^{1/3}, \theta_r] & \text{if } u_s < 0 \end{cases} \quad (6)$$

In Eq. (6), k_a and k_r are empirically determined material parameters [29,30] for the advancing and receding contact angles, respectively. While the model was developed for flat

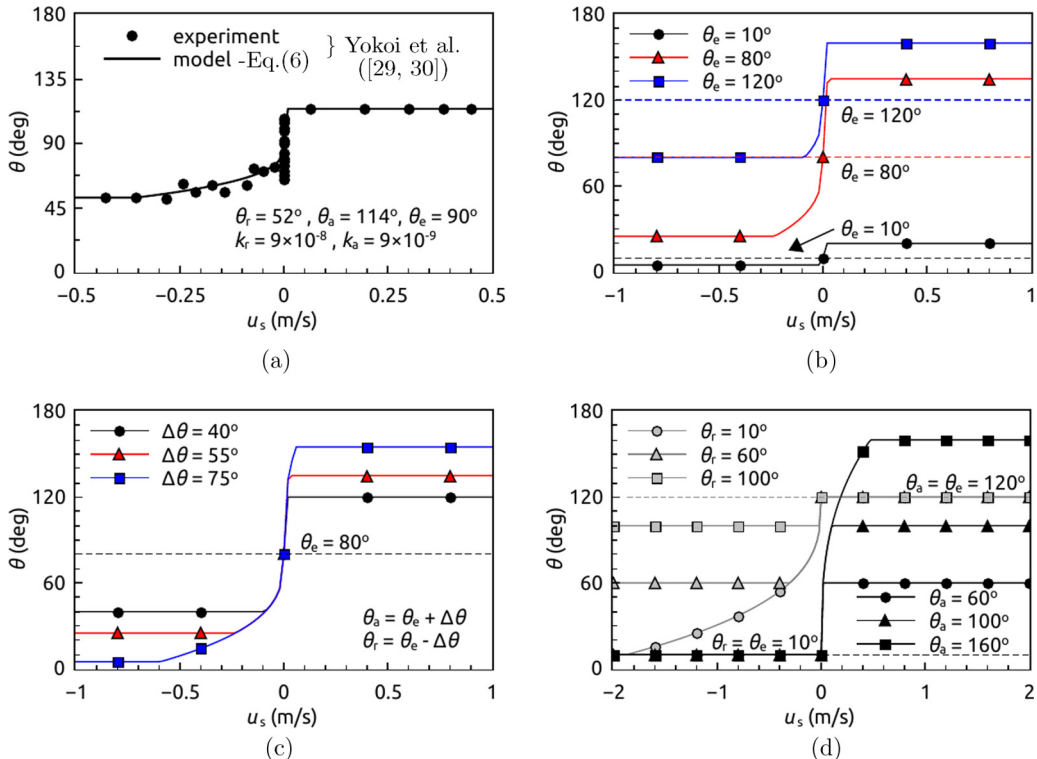


FIG. 3. Dynamic contact angle model from (a) Yokoi *et al.* [29,30] and (b) the various combinations of equilibrium, advancing and receding contact angles considered for the parametric analysis in this study; for (b–d) $k_a = 10^{-7}$ and $k_r = 10^{-6}$.

solid surfaces, the relationship is expected to hold for curved surfaces, such as fibers, where the contact angles are evaluated with reference to the local tangent [62,63] at the three-phase contact line. It is noted that static contact angle hysteresis is implicitly accounted for in the present dynamic contact angle model, through the parameters k_a and k_r , where the local contact angle can still vary significantly with minimal variation in the wetter area for $|\mu_s| \rightarrow 0$. In this study, the influence of wetting dynamics is investigated in two parts: (i) influence of contact angle hysteresis for given equilibrium contact angles, and (ii) effect of contact angle (each with a specified hysteresis). An example for determining k_a and k_r according to Eq. (6) is shown in Fig. 3(a), and the further models based on Eq. (6) that are used for the parametric analysis are shown in Figs. 3(b)–3(d). Three different groups of static and dynamic contact angle combinations are studied—different equilibrium contact angles with zero or specified hysteresis [Fig. 3 (b)], a range of equivalent advancing and receding hysteresis for a given equilibrium contact angle [Fig. 3(c)], and superoleophilic or phobic fibers with varying levels of advancing or receding hysteresis [Fig. 3(d)] to isolate their influence on the dynamics of droplet-fiber interaction. In the following sections, the term “contact angle hysteresis” indicates the maximum extent of contact angle hysteresis or the difference between limiting advancing and receding contact angles [64–66], unless explicitly specified otherwise.

IV. VALIDATION OF COMPUTATIONAL TECHNIQUE

While the VOF methodology in interFOAM has been widely validated for multiphase simulations in the literature [54–56,70], few studies involve the (small) length scales considered in this work. The CFD methodology used in this study, along with the contact angle models employed for the simulations, are validated against several theoretical and experimental data sets from the literature [29,56,67,68], encapsulating both static as well as dynamic droplet wetting conditions and processes. The first data set corresponds to 2D sessile droplets placed on a flat and cylindrical surfaces (see inset in Fig. 4) such that the droplets equilibrate from an initial shape given by the droplet height $h = d/2$ to a final shape dependent on the static contact angle θ_e . The simulations were carried out with $\rho_l = 1000 \text{ kg/m}^3$, $\mu_l = 10^{-3} \text{ Pa s}$, $\rho_g = 1 \text{ kg/m}^3$, $\mu_g = 10^{-5} \text{ Pa s}$, and $\sigma = 0.01 \text{ N/m}$, following Fakhari and Bolster [67]. Figure 4 compares the present predictions of the dimensionless equilibrium droplet heights (h/d) against the theoretical and computational (LBM) predictions from Fakhari and Bolster [67], for different contact angles. It is seen from the figure that the predicted droplet shapes are in excellent agreement with the literature over the entire range of contact angles, covering both philic and phobic surfaces.

The second data set considered for validation corresponds to the breakup of a thin liquid film around a microfiber due to Plateau-Rayleigh instability [56,68]. The present computations are carried out using a thin film of DEHS (surrounded by air) of different initial film heights $h_o > d_f/\sqrt{2}$ [71] coated on microfibers of various diameters d_f . Figure 5(a) shows the comparison in the equilibrium spacings (d_{sp}) between the droplets against analytical, experimental and computational

data from Kalliadas and Chang [69], Haefner *et al.* [68] and Mead-Hunter *et al.* [56], respectively. A comparison of the transient variations in the dimensionless growth rate of the instability (that eventually form the droplets) between the present simulations and Haefner *et al.* [68] is shown in Fig. 5(b). The arrangements of droplets at various instants are also visualized in Fig. 5(b). It is seen from the Fig. 5(a) that the predicted droplet spacings are in excellent agreement with the literature. Though the measurements of Haefner *et al.* [68] involved molten entangled polystyrene, and the present simulations used DEHS ($\rho_l = 912 \text{ kg/m}^3$, $\mu_l = 0.0228 \text{ Pa s}$ and $\sigma = 0.032 \text{ N/m}$), the predicted dimensionless growth rate in Fig. 5(b) compares well with the measurements [68], reinforcing the validity in the present methodology.

The final exercise involves the validation of the customized implementation of the dynamic contact angle model from Yokoi *et al.* [29] into OpenFOAM. This is carried out by evaluating the dynamics of wetting of a droplet impacting a stationary flat surface—a case that was originally used in Yokoi *et al.* [29] for the development of the dynamic contact angle model. A droplet of water ($\rho_l = 1000 \text{ kg/m}^3$, $\mu_l = 10^{-3}$) falls due to the influence of gravity, in an ambience of air ($\rho_g = 1.25 \text{ kg/m}^3$, $\mu_g = 1.82 \times 10^{-5}$) and impacts a flat surface at a velocity $u_o = 1 \text{ m/s}$. The contact angle between water and the surface is as shown in Fig. 3(a), and the air-water interfacial tension is assumed to be 0.072 N/m . The comparison between the predicted wetted diameter (calculated as $d_w = \sqrt{4A_w/\pi}$) where A_w is the wetted area) and experimental data [29] is shown in Fig. 6. Instantaneous shapes of the droplets at different times are also shown in the figure and compared with the photographs in Yokoi *et al.* [29]. It can be seen in the figure that the predictions from the present methodology are in good agreement with the literature, thereby validating the incorporated dynamic contact angle model for the study, and reaffirming the validity of the present computational approach.

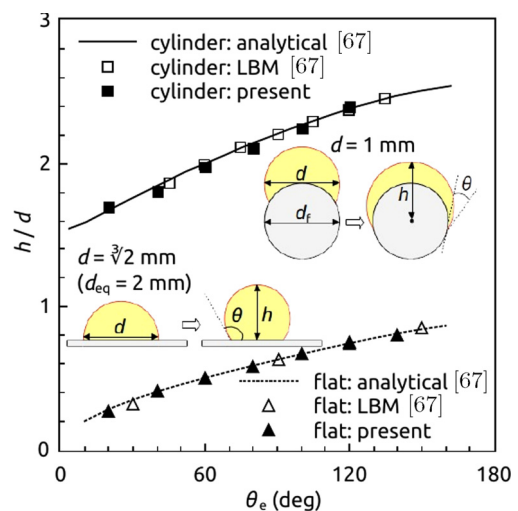


FIG. 4. Comparison of predicted dimensionless heights of sessile drops on flat and cylindrical surfaces, for different static contact angles, against theoretical and lattice Boltzmann simulation results from Fakhari *et al.* [67].

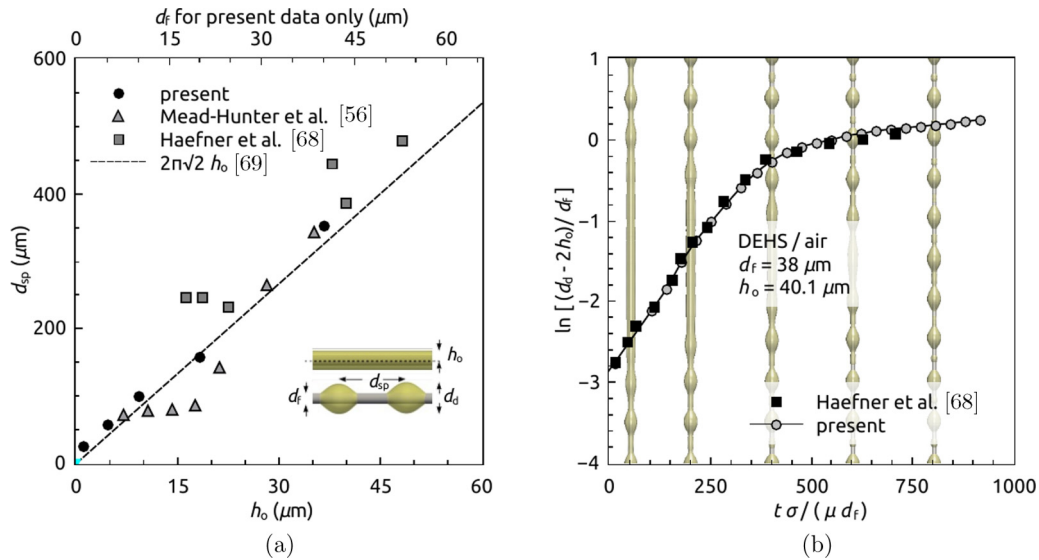


FIG. 5. Comparison of (a) droplet spacing and (b) droplet growth rate during Plateau-Rayleigh instability, predicted by the present CFD methodology, against the theoretical, experimental, and computational data in the literature [56,68,69].

V. RESULTS AND DISCUSSION

The relative significance of wetting properties on the capture or re-entrainment of a microdroplet impacting or intercepting a fiber of mist filter is investigated under different operating conditions (free-stream velocities, droplet-fiber offset and diameter ratios). The potential for the retention of a captured droplet under the dynamic conditions is also quantified in terms of the dimensionless area wetted by the droplet upon contact with the fiber, and qualitatively characterized from visual representation of the results from CFD. The latter is pertinent as any observed low wetted area can be due to the phobicity or rather deceptively, partial capture or re-entrainment, as can be seen in the following sections.

A. Head-on droplet-fiber impaction

The simplest configuration involving the impact of a droplet on fiber corresponds to $W = 0$ which, under steady free-stream flow conditions, results in droplet capture [72]. Figure 7(a) illustrates the variation in the dimensionless wetted area given by $A = A_w/(\pi d^2/4)$ and droplet height for three equilibrium contact angles $\theta_e = 10^\circ, 80^\circ$ and 120° (each with associated hysteresis), and Fig. 7(b) shows the corresponding evolution in droplet shapes for two representative cases at different time points (given by the dimensionless time $\tau = u_o t/d$). The droplet height h is calculated as shown in Fig. 4. The dimensionless contact area and the height for the three diameter ratios $R = 1, 2,$ and 3 considered for the study (only $R = 1$ and 2 are shown in the figure for clarity) were found to collapse for empirical functions of R (obtained by correlating the dataset generated in the present study) as shown in the ordinates of Fig. 7(a). It can be seen from the figures that there are at least three distinct regimes of droplet-fiber interactions: Kinetic energy or inertia controlled spreading [21,22], capillary and contact angle controlled spreading and retraction [23,24] and upstream stagnation pressure-induced viscous spreading, until equilibrium is attained. Unlike typical droplet impact scenarios in quiescent mediums which involve only the first two stages [31], the presence of a surrounding flow [32] results in third stage of spreading of the droplet on the cylinder. It can be seen from Fig. 7(a) that rate of spreading under the third stage is considerably lower than that during the inertia dominated stage. Figure 7(a) also shows that the transient variation in the dimensionless wetted area between $\theta_e = 80^\circ$ and 120° during rapid spreading (kinetic) are nearly equivalent, but substantially differ during the third stage where the droplet spreads more slowly. Recalling the contact angle model in Fig. 3, the dynamics of droplet spreading is controlled by θ_a in the stages where $u_s \gg 0$ (kinetic) and by θ_e during the slower spreading process. Since the advancing contact angles are nearly equivalent ($\theta_a = 155^\circ$ and 160°) between the two cases

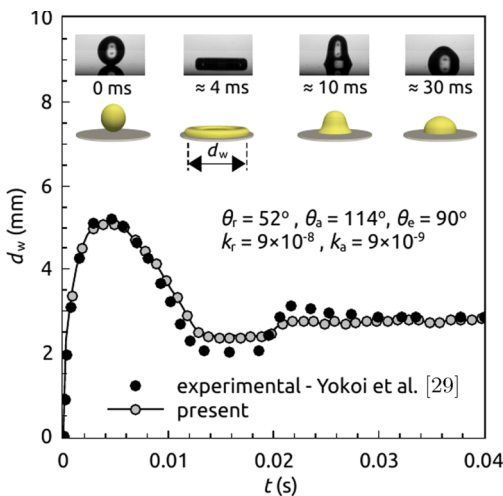


FIG. 6. Comparison of the transience in predicted equivalent wetted diameter on the impingement surface against Yokoi *et al.* [29]; photographs of the droplet shapes [29] are shown above the predicted shapes obtained in the present study.

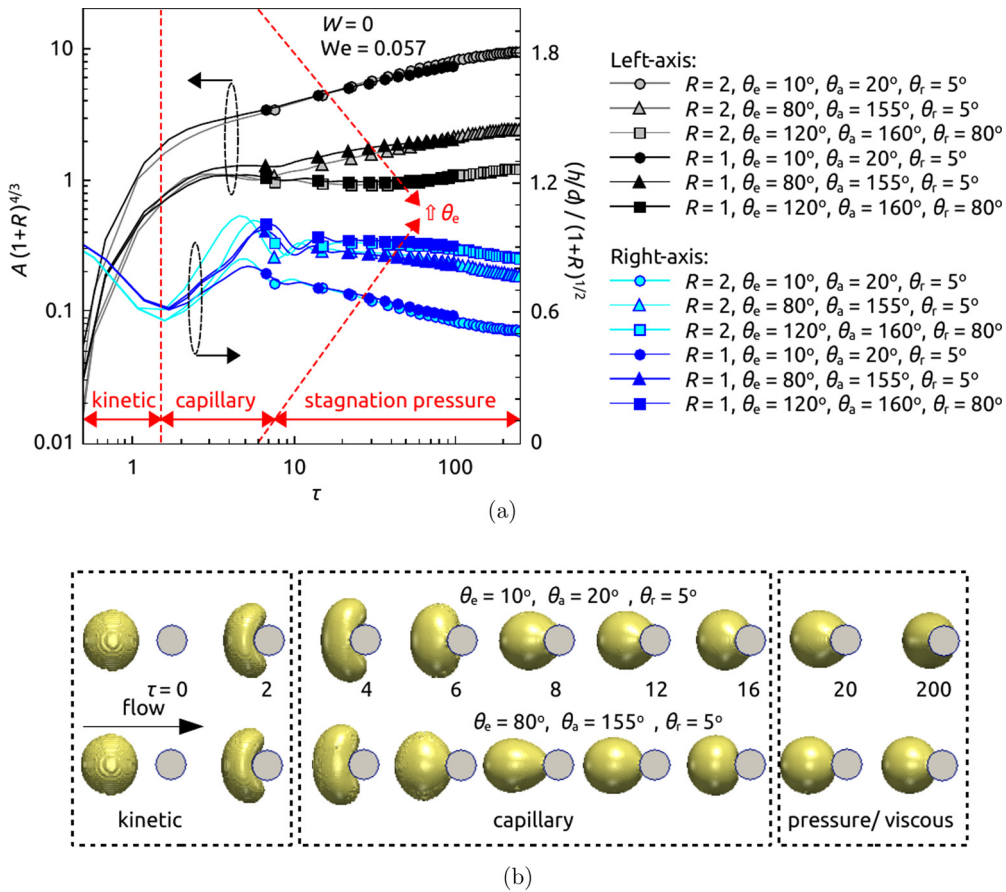


FIG. 7. Influence of contact angle on the characteristics of head-on droplet impact: (a) dimensionless wetted area and droplet height for different droplet-fiber diameter ratios and (b) droplet shapes during the three stages of head-on impaction.

considered ($\theta_e = 80^\circ$ and 120°), the transience in the wetted area in the inertia controlled rapid spreading stage are nearly equivalent between the two cases. However, the differences in θ_e itself between the two cases contributes to the difference in the rate and magnitude of spreading in the third phase.

It is also interesting to note in Fig. 7(a) that the oscillations in the droplet height are more prominent than the same in wetted area during the capillary controlled phase. While the duration of the inertial spreading phase is nearly independent of the equilibrium contact angle, it can be seen that the transition from the capillary driven droplet dynamics phase is greater for greater contact angles. This can be attributed to the fact that greater contact angles invariably result in greater droplet heights because of the simultaneous effects of lower wetted area and surface tension. When the surface energy of the fiber is lower, i.e. high contact angles, the tendency of the droplet to spread is weaker, than the surface tension force that seeks to minimize the surface area of the liquid. The greater droplet height, compounded by the greater hysteresis at the contact line results in the oscillations to last longer for greater contact angles. The duration of the capillary controlled stage is determined by the total momentum in the droplet, as some of it is continuously absorbed and redistributed for the spreading of the droplet on the fiber, until the viscous effects make the oscillations insignificant and the droplet continues to spread due to the upstream stagnation pressure induced due to the air flow.

Given that $(1 + R)^{4/3}$ increases with the droplet to fiber diameter ratio R , Fig. 7(a) also implies that the wetted area on the cylinder decreases with an increase in R , irrespective of the contact angle. This is indicative that droplet retention potential on the fiber is greater for filter media with larger fibers. This observation is however not extensible to relate R with particle capture efficiency—which is undoubtedly lower for greater fiber diameters [7], for any given packing density or droplet diameter. Figure 7(a) also indicates that an increase in phobicity for oil on the filter surface (or increase in θ_e) results in a concomitant reduction in the wetted area irrespective of the other operating conditions considered. Consequently, the droplet heights are consistently greater for greater equilibrium contact angles.

The influence of contact angle hysteresis on the wetted area and droplet height is illustrated in Fig. 8 for a representative equilibrium contact angle $\theta_e = 80^\circ$ and the other operating conditions given by $R = 2$, $We = 0.057$, and $W = 0$. For simplicity, the difference between the advancing or receding and equilibrium contact angles is kept the same ($\Delta\theta = \theta_e - \theta_r = \theta_a - \theta_e$) for the cases shown in Fig. 8. It can be seen from the figure that, irrespective of the droplet-fiber interaction regime (discussed in Fig. 7), the dimensionless wetted area is consistently lower, and the droplet height is consistently greater, for higher $\Delta\theta$. In the initial spreading stage, for example, $0.5 \lesssim \tau \lesssim 1.5$ or $5 \lesssim \tau \lesssim 8$, an increase in $\Delta\theta$ results in greater deformation of the droplet upon

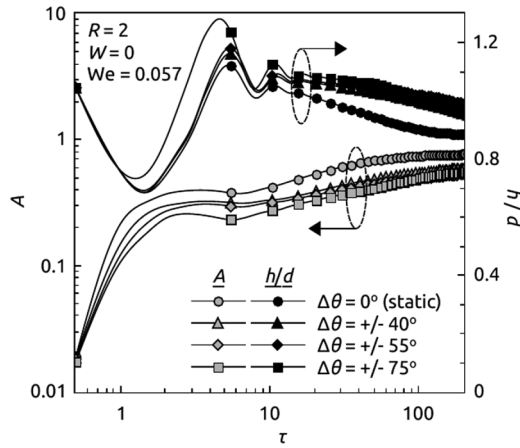


FIG. 8. Influence of wetting hysteresis on the characteristics of head-on droplet-fiber impact on the dimensionless contact area and droplet height, for $\theta_e = 80^\circ$.

impact (or greater curvature adjacent to the fiber surface), due to the greater contact angle (θ_a) that is accommodated at the contact line, for a given initial droplet velocity. However, for lower θ_a , the kinetic energy of the impacting droplet is utilized for greater spreading on the fiber surface. In the droplet retraction stage, for example $1.5 \lesssim \tau \lesssim 5$, the lower receding contact angles for greater values of $\Delta\theta$ results in the faster recoil of the droplet surface at the contact line, thus resulting in the fluid inside the droplet to be sprung toward its center. As a consequence, the droplet heights are greater for lower values of θ_e during droplet recoil. The reduction in amplitude of droplet oscillations (such as in the droplet height) are generally attributed to the energy dissipation due to viscous forces [33]; however, the presence of a surrounding flow can further suppress the oscillations, due to the upstream stagnation pressure that acts as an additional resistance to the recoil. Figure 8 also shows that since θ_a is the same for the

cases considered, A and h/d both tend to converge for all the values of wetting hysteresis ($\Delta\theta$) considered here.

B. Influence of contact angle hysteresis—Impaction and interception

The isolated influence of advancing or receding contact angles on the dynamics of an impacting microdroplet is illustrated in Figs. 9(a) and 9(b) for $R = 2$, $S = 0.75$, $We = 0.057$, and two representative equilibrium contact angles 10° and 120° , respectively. An increase in θ_a for a given value of θ_r , or a decrease in θ_r for a given value of θ_a , both result in increasing the contact angle hysteresis ($\Delta\theta = \theta_a - \theta_r$). However, it is seen from the Figs. 9(a) and 9(b) that an increase in the hysteresis has contrasting influence on the wetted area and the dynamics of the droplet progression around the fiber, between the two cases. As outlined earlier, an increase in the advancing contact angle results in the accommodation of greater curvature on the advancing section of the three-phase contact line on the fiber (analogous to pinning the front end of the droplet to the fiber) and thus results in an associated consistent reduction in the wetted area. On the contrary, lowering of the receding contact angle tends to have the same influence on the receding section of the contact line (by resisting the progression of the droplet’s receding end) thus resulting in an associated increase in the wetted area. The recoil of the droplet due to surface tension, compounded by the curvature of the fiber over which the droplet traverses, results in the increased reduction in A with an increase in the advancing hysteresis ($\theta_a - \theta_e$). In congruence, a lesser reduction in A is seen with increase in the receding hysteresis ($\theta_e - \theta_r$). Hence, the key inference from Figs. 9 (a, b) is that contact angle hysteresis plays a dual role depending on the individual limiting contact angles. Large contact angle hysteresis on a philic fiber can be detrimental for droplet capture while the same on a phobic media can be beneficial for capture. This is due to the fact that a larger hysteresis for a generally philic fiber results greater advancing contact angles (or relative decrease in contact area)

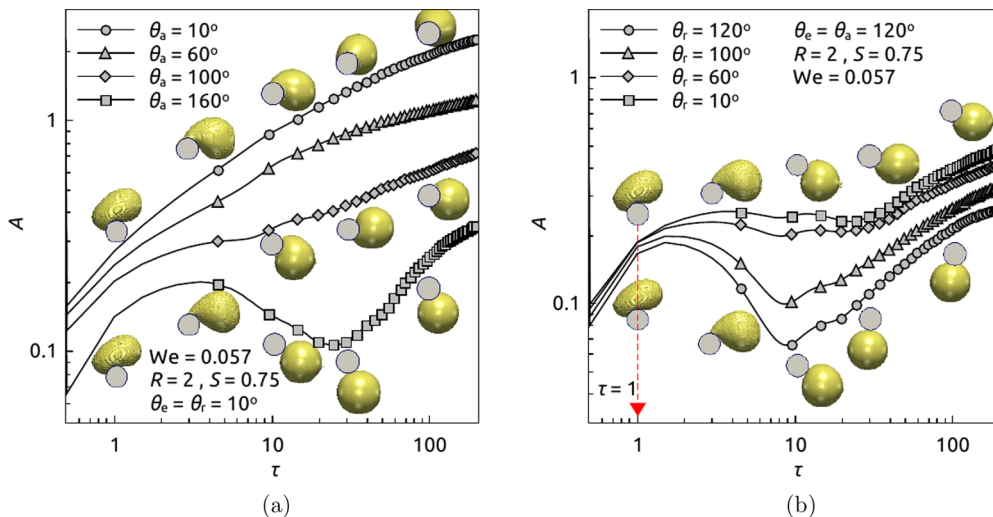


FIG. 9. Influence of contact angle hysteresis in the form of isolated variations in the (a) advancing or (b) receding contact angles, on dimensionless wetted area; droplet shapes at different dimensionless times are shown, where the center of the fiber indicates the corresponding value of τ as illustrated in (b).

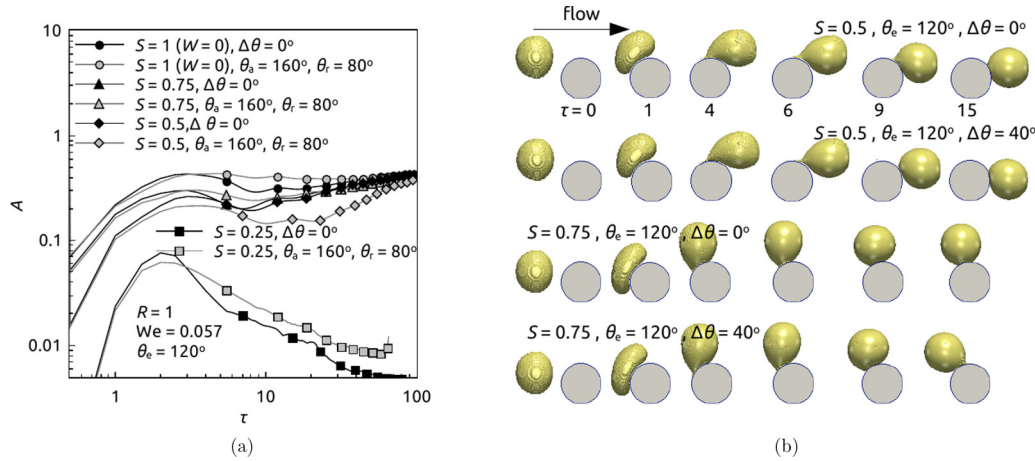


FIG. 10. Relative influence of contact angle hysteresis under different initial apparent droplet-fiber overlaps on the (a) transient evolution of the dimensionless contact area, and (b) droplet-fiber interaction; the different instances shown in (b) correspond to $\tau = 0, 1, 4, 6, 9$, and 15 .

when the droplet is in motion around the fiber, while the same for a phobic fiber results in the reduction in the receding contact angle (or relative increase in wetted area).

The role of contact angle hysteresis under different droplet-fiber apparent overlaps (or offsets) is explored in Fig. 10. Four overlaps corresponding to $S = 0.25, 0.5, 0.75$, and 1 are considered, for a given set of operating conditions $R = 1$, $We = 0.057$, equilibrium contact angle $\theta_r = 120^\circ$, and contact angle hysteresis $\Delta\theta = 0^\circ$ or 40° . The equilibrium contact angle for all cases is 120° , corresponding to a poorly wettable (and superphobic) fiber. The transient variation in the dimensionless wetted area for the eight cases are shown in Fig. 10(a), and the evolution of droplet shapes for two representative cases are shown in Fig. 10(b). It is seen from the Fig. 10(a) that the zero, low, and moderate offset cases ($S = 0.5$ to 1) approach similar equilibrium contact areas with time; however, there is significant variation in the instantaneous wetted area during the initial stages of capture, i.e., in the inertial and capillary controlled stages. From Fig. 10(b), we can also see the influence of droplet offset, where the droplet may end up on the top or rear of the fiber. At greater offsets (or lower overlaps), the initial contact of the droplet on the fiber is smaller in area, and momentum acts to move the droplet over the surface of the fiber, until this force is diminished and the adhesion force predominates. This can be seen in the visualization in Fig. 10(b), where the cases with $S = 0.5$ result in the droplet adhering to the rear of the fiber.

Conditions involving greater droplet fiber offsets can often result in noncapture or partial capture. The lower apparent overlap for the representative case with $S = 0.5$ discussed in Fig. 10, is sufficient to reduce the size of the initial contact area to the extent that no effective adhesion force is present. However, it is interesting to note from Fig. 10(a) that contact angle hysteresis acts both favorably as well as adversely on the initial stages of the droplet-fiber interaction, depending on the initial droplet-fiber overlap S . It can be seen from Fig. 10(a) that, during the capillary phase ($2 \lesssim \tau \lesssim 40$), the dimensionless wetted area for $\Delta\theta = 40^\circ$ is greater than that for $\Delta\theta = 0^\circ$ for $S = 1$, while the same is lower for $S = 0.5$, and nearly equal for $S = 0.75$ —indicating a clear shift in the trend. This can be attributed to the interplay between the

asymmetry in the spreading and progression of the droplet around the fiber. For perfectly centered impact cases ($S = 1$), the droplet spreads uniformly on either side of the fiber upon impact, with all contact lines either advancing or receding as the impact and restitution progresses. For offset impact, there is an imbalance or asymmetry in motion of the contact line, and for greater offset it is increasingly likely that advancing and receding contact lines can occur simultaneously. Contact angle hysteresis (or not) serves to amplify the difference between cases at lower values of S , provided break-up or detachment does not occur. As one can expect, lower initial overlaps such as $S = 0.25$ shown in Fig. 10 results in the re-entrainment of the droplet into the stream. The small nonzero dimensionless wetted area A seen in Fig. 10(a) for $S = 0.25$, $\Delta\theta = 40^\circ$ is due to partial capture of the droplet on the fiber.

Figures 11(a) and 11(b) illustrate the effect on droplet (and free-stream) velocity (in terms of We) on the capture process. At the lower value of We ($=0.01425$), in the absence of contact angle hysteresis, we can see that the droplet is captured. However, when contact angle hysteresis is nonzero, despite the fiber being oleophilic, it can be seen from Figs. 11(a) and 11(b) that the droplet is re-entrained into the flow, however with a small fraction of the droplet retained on the fiber resulting in partial capture. This is seen as the nonzero dimensionless area for $We = 0.01425$ (grey triangles). The interplay between the local flow field, dynamics of the droplet movement on the fiber and point of detachment of the droplet can sometimes result in the re-capture of a re-entrained droplet as seen in Fig. 11(b) for $We = 0.01425$ (with hysteresis) at $\tau = 8$. An associated increase in A can be seen in Fig. 11(a). It is also seen from the representative cases for $We = 0.057$ shown in the figures that the influence of contact angle hysteresis is of lesser significance for greater values of We . This is because, at higher values of We , momentum of the droplet and drag exerted by the surrounding air that carries the droplet, are far greater for the resistance offered by the surface adhesion forces to retain the captured droplet. It can also be extrapolated that the probability of capture of a droplet moving at a high values of We will be lesser for lower initial apparent overlaps—notice the reduction in the peak value of A

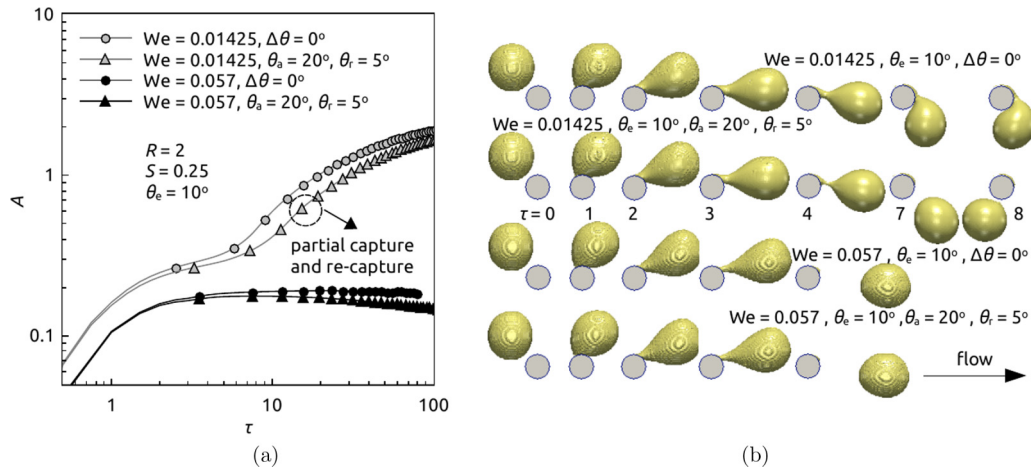


FIG. 11. Relative influence of contact angle hysteresis under different droplet Weber numbers, on the (a) transient evolution of the dimensionless contact area and (b) droplet-fiber interaction; the different instances shown in (b) correspond to $\tau = 0, 1, 2, 3, 4, 7, \text{ and } 8$.

with S at the end of the impaction stage in Fig. 10(a). This has implications for droplet capture processes, and specifically affects interceptional capture efficiency.

Figures 12(a) and 12(b) illustrate the relative influence of contact angle hysteresis for varying droplet-fiber diameter ratios and for $We = 0.01425, S = 0.5, \text{ and } \theta_e = 80^\circ$. It is seen from the figures that the dimensionless wetted area is greater for $R = 1$ as compared to $R = 2$ for the entire duration of the droplet-fiber interaction, irrespective of contact angle hysteresis. An increase in the hysteresis is also seen to be particularly detrimental for droplet capture for the lower fiber diameter; for example, $\Delta\theta = 50^\circ \text{ and } 75^\circ$ for $R = 2$ results in re-entrainment as seen in Figs. 12(a) and 12(b). It is noted that the relationship between R and droplet capture or re-entrainment that is discussed in this section does not reflect the overall capture efficiencies of a fibrous filter as the variation in the overall packing density due to variation in fiber diameter is not accounted for in this section. Nevertheless, the efficiency of droplet capture based on the single fiber efficiency theory

[7] can be an overestimate as the re-entrainment of a captured droplet is not accounted therein.

C. Influence of equilibrium contact angle in the absence of hysteresis

To isolate the influence of wettability in terms of the equilibrium contact angle alone, simulations are carried out by varying θ_e in the range 10° to 120° , encompassing the spectrum of filters from oleophilic to oleophobic, and in the absence of contact angle hysteresis. Figures 13(a) and 13(b) show the influence of equilibrium contact angle on the transience in the droplet-fiber impact dynamics for two initial apparent overlaps given by $S = 0.25$ and 0.5 . It can be seen from the figures that the dimensionless contact area decreases, as expected, with an increase in θ_e owing to reduced wettability. It is also seen that, for the superoleophobic ($\theta_e = 120^\circ$) media, re-entrainment occurs only for $S = 0.25$ while the droplet is captured and retained on the fiber for

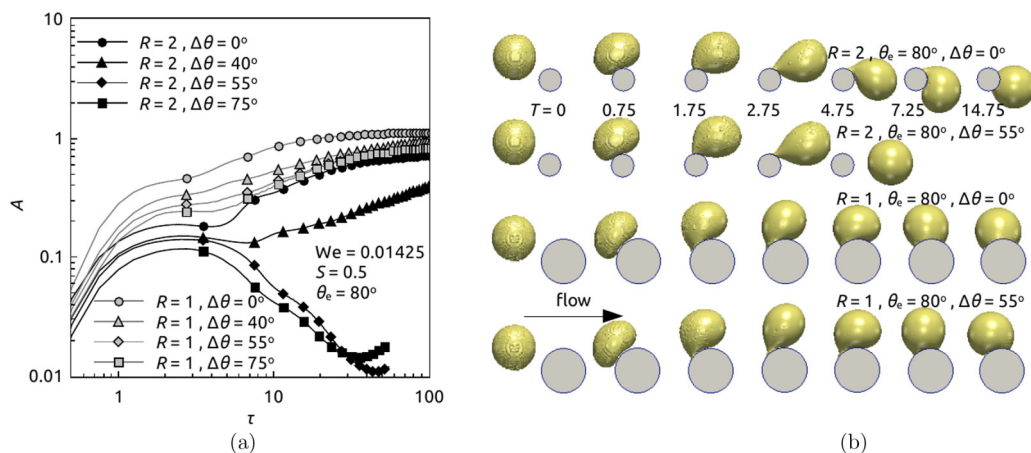


FIG. 12. Relative influence of contact angle hysteresis under different droplet-fiber diameter ratios, on the (a) transient evolution of the dimensionless contact area and (b) droplet-fiber interaction; the different instances shown in (b) correspond to $\tau = 0, 0.75, 1.75, 2.75, 4.75, 7.25, \text{ and } 14.75$.

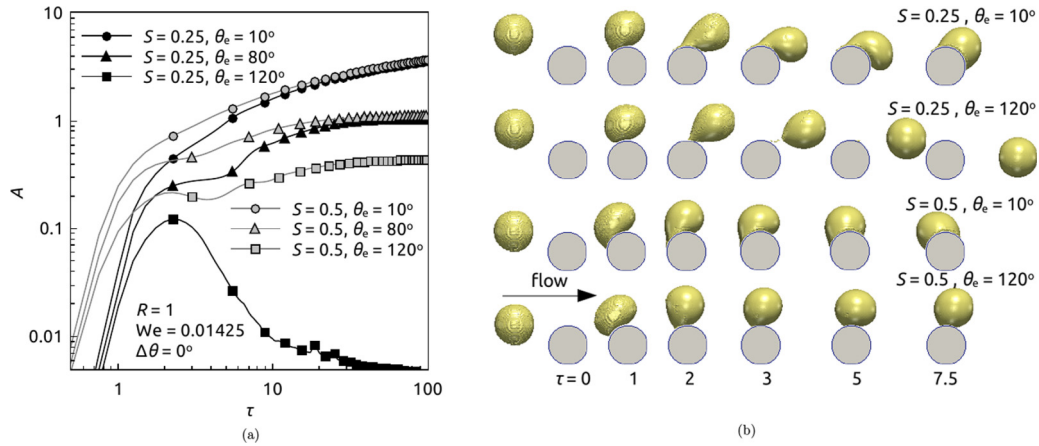


FIG. 13. Relative influence of equilibrium contact angle under different initial apparent droplet-fiber overlaps, on the (a) transient evolution of the dimensionless contact area and (b) droplet-fiber interaction; the different instances shown in (b) correspond to $\tau = 0, 1, 2, 3, 5,$ and 7.5 .

$S = 0.5$. This observation, and the comparison of the images for the phobic filter ($\theta_e = 120^\circ$) between $S = 0.25$ and 0.5 shown in Fig. 13(b) indicate that an increase in S increases the likelihood of droplet capture for all contact angles. It is also important to note that while the droplet remains captured for $S = 0.5, \theta_e = 120^\circ$, the lower contact area (compared to lower values of θ_e) at steady state indicates that in many real situations, which involve dynamic velocity fluctuations, droplet re-entrainment may occur due to the relatively lower force required for droplet detachment [73].

The influence of equilibrium contact angle on the dynamics of droplet capture or re-entrainment under different flow velocities (or We) is illustrated in Figs. 14(a) and 14(b). Since higher values of We indicate higher droplet momentum as well as surrounding flow velocities, a concomitantly greater adhesion force is necessary for the retention of a droplet that has impacted or has been intercepted by the fiber. Since adhesion forces are lower for greater contact angles, this indicates that the increase in We invariably compounds the effect of low wettability and increases the possibility of re-

entrainment. This is evident from Figs. 14(a) and 14(b) where, besides the reduction in wetted area with increase in θ_e , droplet detachment occurs at $\theta_e = 80^\circ$ for $We = 0.057$ but re-entrainment occurs only at $\theta_e = 120^\circ$ for $We = 0.01425$.

The influence of equilibrium contact angle on the transient variation in the dimensionless wetted area and the interaction between the droplet and fiber, under the absence of hysteresis, for varying droplet-fiber diameter ratios is shown in Figs. 15(a) and 15(b). Here, larger droplet-fiber ratios are considered at three different equilibrium contact angles, covering the spectrum from philic to super phobic. As observed in the previous section discussing the significance of contact angle hysteresis, Figs. 15(a) and 15(b) show that an increase in R enables greater contact between fiber and the oncoming droplet, irrespective of the droplet-fiber wettability. This increase in contact area results in an associated increase in the frictional resistance to the traversal of the droplet on the fiber, thereby favoring capture. It is hence seen in Figs. 15(a) and 15(b) that while $R = 4$ results in re-entrainment for $\theta_e = 120^\circ$, droplet remains captured for the counterpart ($R = 2$).

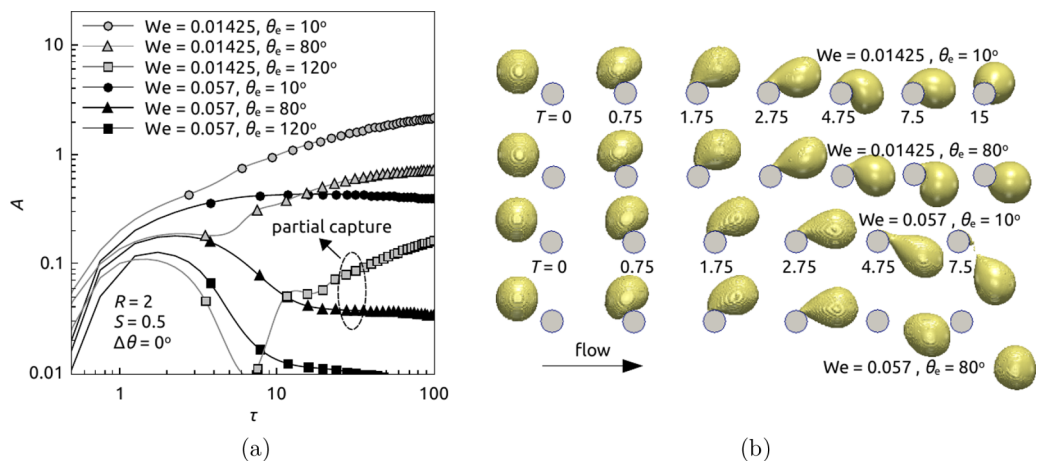


FIG. 14. Relative influence of equilibrium contact angle under different droplet Weber numbers, on the (a) transient evolution of the dimensionless contact area and (b) droplet-fiber interaction; the different instances shown in (b) correspond to $\tau = 0, 0.75, 1.75, 2.75, 4.75, 7.5,$ and (for $We = 0.01425$) 15 .

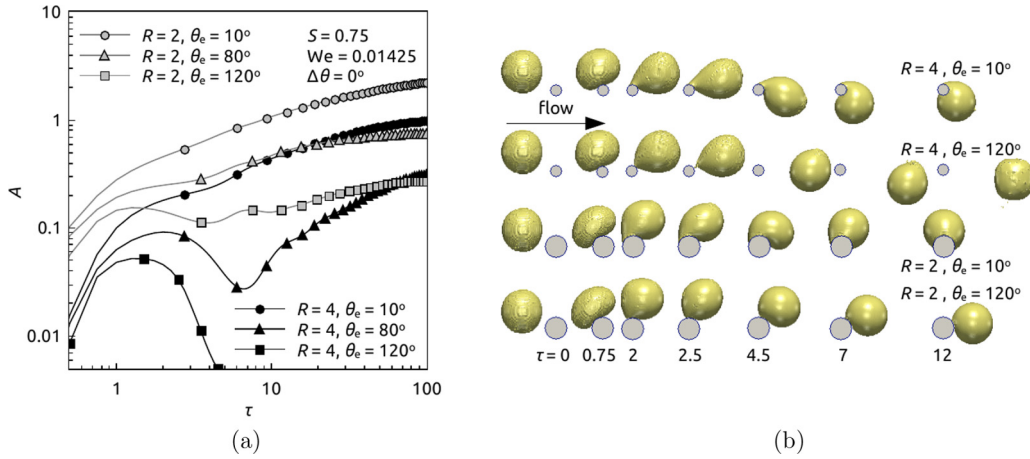


FIG. 15. Relative influence of equilibrium contact angle under different droplet-fiber diameter ratios, on the (a) transient evolution of the dimensionless contact area and (b) droplet-fiber interaction; the different instances shown in (b) correspond to $\tau = 0, 0.75, 2, 2.5, 4.5, 7$, and 12.

D. Significance of wettability for filter design

First, both static and dynamic wetting properties play key roles in microdroplet (mist) filtration process, and filter media manufacturers must take this into consideration for optimizing filtration performance. While most filters intended for oil or water filtration and separation are hydro- or oleophilic, there has been a recent interest and increase in the use of phobic media due to their reduced pressure-drop [3] and even potentially greater capture efficiencies [4,5]. Second, the classification of filtration media for any fluid system, rather broadly, as philic or phobic (based on the static contact angle) may be insufficient for two reasons: (i) the behavior of filters varies widely over the possible range of contact angles and operating conditions; and more importantly; (ii) the equilibrium contact angle plays little role in the initial stages of the droplet-fiber interaction which is found to dictate the fate of the droplet in most cases. On the contrary, it is the contact angle hysteresis that influences the initial stages of droplet impact on fibers the most—however, commercial filters are seldom characterized based on this property. Finally, computational modeling is increasingly becoming an integral part of design of filter media [1,41,42] and its efficacy is greatly dependent on the accuracy of material properties, such as wettability, used in the simulations. Characterization of filters based on more accurate wetting properties are inherently essential for better optimization, although it is known that the measurement even the static contact angles on micro- or nanofibers is still a significant challenge [44–47].

The most widely used tool for predicting the performance of mist and dust filters is the classical single-fiber theory [7] which assumes that a particle (mist or dust) is captured as soon as it comes in contact with the fiber. However, several studies for dust [11–18] and mist filters [4,8] have found that this is not true. To the authors' knowledge, the present work is the first attempt at investigating the influence on contact angle dynamics on single particle (droplet)-fiber interaction. This work has highlighted the importance of characterizing filter media based on the contact angle dynamics on some of the mechanisms that can result in the deviations from predictions in SFE theory. Further controlled experiments or a series of

simulations with isolated variation in parameters over a wider range of operating conditions are required to empirically correlate capture efficiency with wettability. However, it is evident that the total capture efficiency for mist droplets must be evaluated as

$$E_{\Sigma} \simeq E_R + E_I + E_D + E_{DR} + E_G - f(\theta_e, \theta_a, \theta_r), \quad (7)$$

where $f(\theta_e, \theta_a, \theta_r)$ is always positive and accounts for droplet re-entrainment after initial capture, due to the influence of contact angle dynamics. The variables E_{Σ} , E_R , E_I , E_D , E_{DR} , and E_G are defined in their conventional way [7] as the total single fiber efficiency and the individual contributions due to interception, impaction, diffusion, interception of diffusing droplets, and gravitational settling, respectively. The nature of the last term in Eq. (7) is such that capture can be estimated or correlated as a function of the contact angles rather having to resolve the impact forces and deformation, for any given value of other parameters such as Weber number or diameter ratio (which are already included in the individual capture efficiency contributions). It is also pointed out that mist capture efficiency can further be reduced for larger mist particles (or mist with greater inertia) due to droplet splitting or slicing [38–40] on upon impaction on a fiber, associated with re-entrainment or partial capture. This is another aspect of mist-fiber interaction that does not occur during dust filtration.

Based on over 200 simulations carried out for the parametric analysis summarized in the preceding sections, representative capture or re-entrainment regime maps are developed, that show the tendency of equilibrium, advancing and receding contact angles, toward droplet capture. Figures 16(a) and 16(b) show the schematics of the transition regimes on two different maps that relate equilibrium contact angle with total contact angle hysteresis [Fig. 16(a)], and that with individual advancing and receding hystereses [Fig. 16(b)]. The parametric analysis suggests that there are at least four distinct regimes: (i) likely capture (philic), (ii) likely particle re-entrainment with minimal or no partial capture (phobic) and which may involve particle bounce [4], (iii) receding contact angle assisted partial or full capture (sticky-phobic),

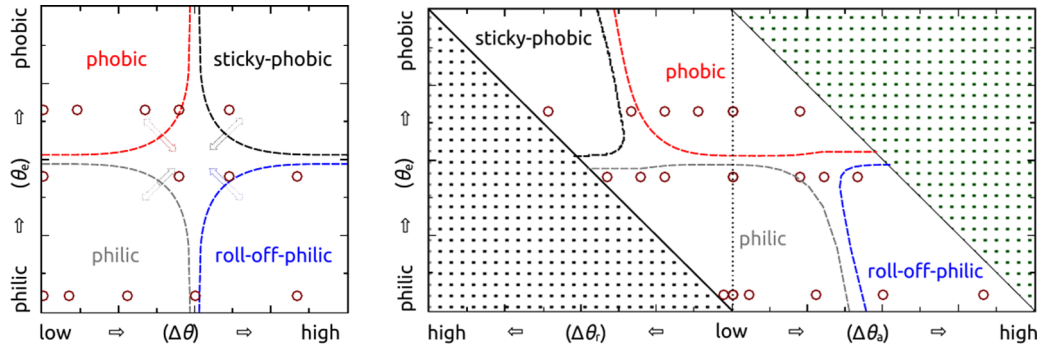


FIG. 16. Capture-regime map, indicating the various droplet-fiber interaction mechanisms; the representative schematics of the transition regimes are shown in two different formats—equilibrium contact angle vs (a) total contact angle hysteresis, and (b) individual advancing and receding hystereses; the contact angles used in the present work are shown with circles.

and (iv) advancing contact angle inhibited partial or full re-entrainment (roll-off-philic). Balu *et al.* [74] discuss a detailed list of the surfaces and materials that can result in the various contact angle combinations discussed in the figure. The terminology for the two contact angle combinations sticky-phobic (high equilibrium contact angle with high receding hysteresis) and roll-off-philic (low equilibrium contact angle with high advancing hysteresis) is also adopted from literature [74,75]. The arrows shown in Fig. 16(a) indicate the direction in which these transition lines may shift with variation in the other operating parameters such as We , R , W , or S . For example, an increase in the droplet-fiber spacing W , the transition regimes are likely to move inwards for the philic and the sticky-phobic regions, but outwards for the phobic and roll-off-philic regions. While a representative schematic is introduced in this work, it is pointed out that further controlled experiments and/or simulations are required with isolated variations in each of the controlling parameters to develop exact maps for different controlling parameters over the range of interest for mist-filtration.

VI. CONCLUSIONS

Computational simulations are carried out using the interface capturing VOF technique, to evaluate the influence of equilibrium contact angle and contact angle hysteresis, on the dynamics of a microdroplet colliding with an isolated fiber during mist filtration. The numerical technique is validated against theoretical and experimental data in the literature [29,56,67,68]. The key findings from the present research are follows:

- (1) In the presence of flow (air carrying the droplet), three distinct regimes of droplet-fiber interactions are present during head-on collision—inertia controlled rapid spreading, capillary controlled spreading and recession (oscillations) and upstream stagnation pressure controlled spreading.
- (2) The key factors characterizing the three collision regimes are: Advancing contact angle determines the extent of initial spreading in the inertial controlled regime, the capillary

stage is influenced by both, advancing and receding contact angles, and the spreading in the third stage is governed by the equilibrium contact angle and gas velocity.

(3) For arbitrary droplet-fiber collisions, irrespective of whether the filter is philic or phobic, all three scenarios viz. full capture, particle capture or re-entrainment, are plausible depending on the other operating parameters such as Weber number, droplet-fiber diameter ratio and droplet trajectory, unlike that assumed in the current SFE theory.

(4) An increase in wetting hysteresis through a reduction in the receding contact angle benefits particle capture, while an increase in advancing contact angle, *ceteris paribus*, increases the possibility of droplet-slide on the fiber and re-entrainment.

(5) Contact angle hysteresis plays contrasting roles depending on the limiting contact angles; large wetting hysteresis for a philic fiber can be detrimental to particle capture while the same for a phobic media can be beneficial for particle capture.

(6) Representative capture or re-entrainment regime maps for mist filtration are introduced, that summarize the parametric analysis carried out in this work into four regions termed as philic, phobic, sticky-phobic, and roll-off-philic.

The role of equilibrium and dynamic wetting properties on the capture or re-entrainment under different operating conditions are further characterized through a parametric analysis for Weber number, droplet-fiber diameter ratio and dimensionless initial droplet-fiber offset (droplet trajectory).

ACKNOWLEDGMENTS

The authors acknowledge the support of Australian Research Council under Linkage Grant No. LP140100919 and Raschig GmbH, Germany, for additional funding. This work was also supported by the Pawsey Supercomputing Centre, Perth, Western Australia with funding from the Australian Government and the Government of Western Australia, through the use of its advanced computing facility and resources.

- [1] S. Abishek, A. J. C. King, R. Mead-Hunter, V. Golkarfard, W. Heikamp, and B. J. Mullins, *Sep. Purif. Technol.* **188**, 493 (2017).
- [2] R. Mead-Hunter, A. J. C. King, and B. J. Mullins, *Sep. Purif. Technol.* **133**, 484 (2014).
- [3] I. E. Agranovski and R. D. Braddock, *AIChE J.* **44**, 2784 (1998).
- [4] X. Wei, F. Chen, H. Wang, H. Zhou, Z. Ji, and T. Lin, *J. Mater. Chem. A* **6**, 871 (2018).
- [5] F. Heuzeroth, J. Fritzsche, and U. A. Peuker, *Particuology* **18**, 50 (2015).
- [6] B. J. Mullins, R. Mead-Hunter, R. N. Pitta, G. Kasper, and W. Heikamp, *AIChE J.* **60**, 2976 (2014).
- [7] W. Hinds, *Aerosol Technology—Properties, Behaviour, and Measurement of Airborne Particles*, 2nd ed. (John Wiley and Sons, New York, 1999).
- [8] J. Conder and T. Liew, *J. Aerosol Sci.* **20**, 45 (1989).
- [9] S. Payet, D. Boulaud, G. Madelaine, and A. Renoux, *J. Aerosol Sci.* **23**, 723 (1992).
- [10] A. Charvet, S. Rolland Du Roscoat, M. Peralba, J. F. Bloch, and Y. Gonthier, *Chem. Eng. Sci.* **66**, 624 (2011).
- [11] B. Dahneke, *Aerosol Sci. Technol.* **23**, 25 (1995).
- [12] H. C. Wang and G. Kasper, *J. Aerosol Sci.* **22**, 34 (1991).
- [13] A. K. Maddineni, D. Das, and R. M. Damodaran, *Powder Technol.* **322**, 369 (2017).
- [14] B. J. Mullins, I. E. Agranovski, and R. D. Braddock, *Aerosol Sci. Technol.* **37**, 587 (2003).
- [15] C.-J. Tsai, D. Y. H. Pui, and B. Y. H. Liu, *Aerosol Sci. Technol.* **12**, 497 (1990).
- [16] G. Kasper, S. Schollmeier, and J. Meyer, *J. Aerosol Sci.* **41**, 1167 (2010).
- [17] H.-C. Wang and W. John, *Aerosol Sci. Technol.* **7**, 285 (1987).
- [18] R. Hiller and F. Loeffler, *Ger. Chem. Eng.* **3**, 327 (1980).
- [19] A. K. Maddineni, D. Das, and R. M. Damodaran, *Sep. Purif. Technol.* **193**, 1 (2018).
- [20] O. V. Kim and P. F. Dunn, *J. Aerosol Sci.* **38**, 532 (2007).
- [21] T. Chenglong, Q. Mengxiao, W. Xinyan, Z. Xuhui, Z. Peng, L. Jianling, and H. Zuohua, *Int. J. Multiphase Flow* **96**, 56 (2017).
- [22] H. Kang, S. D. N. Lourenco, and W. M. Yan, *Phys. Rev. E* **98**, 012902 (2018).
- [23] M. Pasandideh-Fard, Y. M. Qiao, S. Chandra, and J. Mostaghimi, *Phys. Fluids* **8**, 650 (1996).
- [24] D. C. Vadillo, A. Soucemarianadin, C. Delattre, and D. C. D. Roux, *Phys. Fluids* **21**, 122002 (2009).
- [25] C. Guo, J. Sun, Y. Sun, M. Wang, and D. Zhao, *Appl. Phys. Lett.* **112**, 263702 (2018).
- [26] C. Antonini, A. Amirfazli, and M. Marengo, *Phys. Fluids* **24**, 102104 (2012).
- [27] M. Delmas, M. Monthieux, and T. Ondarcuhu, *Phys. Rev. Lett.* **106**, 136102 (2011).
- [28] Y. J. Wang, S. Guo, H.-Y. Chen, and P. Tong, *Phys. Rev. E* **93**, 052802 (2016).
- [29] K. Yokoi, D. Vadillo, D. Hinch, and I. Hutchings, *Phys. Fluids* **21**, 072102 (2009).
- [30] K. Yokoi, *Soft Matter* **7**, 5120 (2011).
- [31] R. Rioboo, M. Marengo, and C. Tropea, *Exp. Fluids* **33**, 112 (2002).
- [32] A. J. Diaz and A. Ortega, *J. Fluids Eng.* **138**, 081104 (2016).
- [33] R. M. Manglik, M. A. Jog, S. K. Gande, and V. Ravi, *Phys. Fluids* **25**, 082112 (2013).
- [34] S. Chun, Z. Chengchun, G. Meihong, L. Xueli, L. Yan, R. Luquan, and A. S. Moita, *Int. J. Heat Fluid Flow* **74**, 89 (2018).
- [35] G. McHale, N. A. Kab, M. I. Newton, and S. M. Rowan, *J. Colloid Interface Sci.* **186**, 453 (1997).
- [36] K. Piroird, C. Clanet, E. Lorenceau, and D. Quere, *J. Colloid Interface Sci.* **334**, 70 (2009).
- [37] E. Lorenceau, C. Clanet, and D. Quere, *J. Colloid Interface Sci.* **279**, 192 (2004).
- [38] S.-G. Kim and W. Kim, *Phys. Fluids* **28**, 042001 (2016).
- [39] E. Dressaire, A. Sauret, F. Boulogne, and H. A. Stone, *Soft Matter* **12**, 200 (2016).
- [40] J. Comtet, B. Keshavarz, and J. W. M. Bush, *Soft Matter* **12**, 149 (2016).
- [41] S. Abishek, A. J. C. King, J. Schuler, G. Kasper, J.-H. Schmid, and B. J. Mullins, *Sep. Purif. Technol.* **207**, 344 (2018).
- [42] R. Mead-Hunter, A. J. C. King, G. Kasper, and B. J. Mullins, *J. Aerosol Sci.* **61**, 36 (2013).
- [43] V. Golkarfard, A. J. C. King, S. Abishek, R. Mead-Hunter, G. Kasper, and B. J. Mullins, *Sep. Purif. Technol.* **213**, 45 (2019).
- [44] B. J. Carroll, *J. Colloid Interface Sci.* **57**, 488 (1976).
- [45] C. Bauer and S. Dietrich, *Phys. Rev. E* **62**, 2428 (2000).
- [46] D. Kampa, S. Wurster, J. Buzengeiger, J. Meyer, and G. Kasper, *Int. J. Multiphase Flow* **58**, 313 (2014).
- [47] T.-H. Yen and C.-Y. Soong, *Phys. Rev. E* **93**, 022805 (2016).
- [48] A. Menchaca-Rocha, A. Martinez-Davalos, R. Nunez, S. Popinet, and S. Zaleski, *Phys. Rev. E* **63**, 046309 (2001).
- [49] M. Ahmadlouydarab, C. Lan, A. K. Das, and Y. Ma, *Phys. Rev. E* **94**, 033112 (2016).
- [50] G. G. Stokes, *Trans. Cambridge Philos. Soc.* **9**, 1 (1850).
- [51] M. Kawaguti, *J. Phys. Soc. Jpn.* **11**, 570 (1956).
- [52] J. Thornburg and D. Leith, *Appl. Occup. Environ. Hyg.* **15**, 618 (2000).
- [53] S. Wurster, D. Kampa, J. Meyer, T. Muller, B. J. Mullins, and G. Kasper, *Chem. Eng. Sci.* **132**, 72 (2015).
- [54] S. S. Deshpande, L. Anumolu, and M. F. Trujillo, *Comput. Sci. Discov.* **5**, 014016 (2012).
- [55] S. Abishek, A. J. C. King, and R. Narayanaswamy, *Int. J. Multiphase Flow* **74**, 148 (2015).
- [56] R. Mead-Hunter, A. J. C. King, and B. J. Mullins, *Langmuir* **28**, 6731 (2012).
- [57] J. U. Brackbill, D. B. Kothe, and C. Zemach, *J. Comput. Phys.* **100**, 335 (1992).
- [58] J. A. Heyns and O. F. Oxtoby, in *Proceedings of the 6th European Conference on Computational Fluid Dynamics* (2014).
- [59] O. Ubbink, Ph.D. Thesis, Imperial College of Science, Technology and Medicine, England (1997).
- [60] O. Ubbink and R. I. Issa, *J. Comput. Phys.* **153**, 26 (1999).
- [61] C. Galusinski and P. Vigneaux, *J. Comput. Phys.* **227**, 6140 (2008).
- [62] Y. Yuan and T. R. Lee, *Surface Science Techniques*, edited by G. Bracco and B. Holst (Springer, Berlin/Heidelberg, 2013).
- [63] M. M. Amrei, M. Davoudi, G. G. Chase, and H. V. Tafreshi, *Sep. Purif. Technol.* **180**, 107 (2017).
- [64] C.-C. Chang, Y.-J. Sheng, and H.-K. Tsao, *Phys. Rev. E* **94**, 042807 (2016).
- [65] C. W. Extrand, *Langmuir* **19**, 3793 (2003).
- [66] G. McHale, N. J. Shirtcliffe, and M. I. Newton, *Langmuir* **20**, 10146 (2004).
- [67] A. Fakhari and D. Bolster, *J. Comput. Phys.* **334**, 620 (2017).

- [68] S. Haefner, M. Benzaquen, O. Baumchen, T. Salez, R. Peters, J. D. McGraw, K. Jacobs, E. Raphael, and K. Dalnoki-Veress, *Nat. Commun.* **6**, 7409 (2015).
- [69] S. Kalliadasis and H. Chang, *J. Fluid Mech.* **261**, 135 (1994).
- [70] S. S. Deshpande, S. R. Gurjar, and M. F. Trujillo, *Phys. Fluids* **27**, 082108 (2015).
- [71] B. J. Mullins and G. Kasper, *Chem. Eng. Sci.* **61**, 6223 (2006).
- [72] S. Abishek, B. J. Mullins, and A. J. C. King, in *Proceedings of the 20th Australasian Fluid Mechanics Conference Perth, Australia* (2016).
- [73] C. Hotz, R. Mead-Hunter, T. Becker, A. J. C. King, S. Wurster, G. Kasper, and B. J. Mullins, *J. Fluid Mech.* **771**, 327 (2015).
- [74] B. Balu, J. S. Kim, V. Breedveld, and D. W. Hess, *J. Adhes. Sci. Technol.* **23**, 361 (2009).
- [75] R. Rincon, A. Hendaoui, J. deMatos, and M. Chaker, *J. Appl. Phys.* **119**, 223303 (2016).